FULL PAPER

Porous Gold with a Nested-Network Architecture and Ultrafine Structure

*Zhen Qi, Ulla Vainio, Andreas Kornowski, Martin Ritter, Horst Weller, Haijun Jin, and Jörg Weissmüller**

A preparation strategy is developed for monolithic samples of nanoporous gold with a hierarchical structure comprising two nested networks of solid "ligaments" on distinctly different structural length scales. The electrochemical dealloying protocol achieves a large retention of less noble element in a first corrosion step, thereby allowing an extra corrosion step which forms a separate structural hierarchy level. The beneficial impact of adding Pt to the Ag–Au master alloys that are more conventionally used in dealloying approaches to nanoporous gold is demonstrated. At ≈6 nm, the lower hierarchy level ligament size emerges extremely small. Furthermore, Pt favors the retention of Ag during the first dealloying step even when the master alloy has a high Au content. The high Au content reduces the corrosion-induced shrinkage, mitigating crack formation during preparation and favoring the formation of high-quality macroscopic (mm-sized) samples. The corrosion effectively carves out the nanoscale hierarchical ligament structure from the parent crystals tens of micrometers in size. This is revealed by X-ray as well as electron backscatter diffraction, which shows that the porous crystallites inherit the highly ordered, macroscopic crystal lattice structure of the master alloy.

1. Introduction

Dealloying is of interest as an approach to fabricate nanoporous metals with a randomly interconnected bicontinuous solid/void structure.[1–6] Several areas of interest in these materials concern processes that require two separate and mutually conflicting properties: Functionality, for instance in the fields of actuators, sensors, or catalysts[7–12] requires large specific surface area and, hence, small pore size. Efficient transport of matter or of signals, by contrast, requires large cross-section of the pore channels and, hence, large pore size. It is well known from phenomena in nature and in man-made systems that structural hierarchy offers a solution to the dilemma.

Previous dealloying approaches toward structural hierarchy include the following: Ding and Erlebacher deposited Ag onto nanoporous gold (NPG), homogenized it at high temperature, and finally implemented a second dealloying step.[13] The approach has remained limited to thin films. Biener et al. suggested the use of ternary alloys, where the two less noble elements are removed in successive corrosion steps.[14] Yet, a successful application of this strategy remains yet to be reported. Zhang et al. used a two-phase master alloys, where the large pores are created by leaching one of the phases.[15,16] This produces bimodal pore structures yet with a low degree of order. Highly ordered hierarchical structures may be prepared by impregnating the pores of templates with the master alloy and then dealloying.[17,18] Again, the approach has remained restricted to comparatively small samples.

A highly ordered hierarchical structure in macroscopic (mm-sized in all dimensions) form has been reported in recent work on nested-network nanoporous gold (N^3PG).[19] The synthesis starts from a dilute solution of Au in Ag and creates nanoporous Ag–Au alloy when only part of the Ag is removed in a first dealloying step. The pore structure is then coarsened by thermal annealing, forming the upper hierarchy level. A second dealloying step finally removes the residual Ag, forming the lower hierarchy level. An unresolved issue with this strategy is the large shrinkage of the sample during corrosion. Shrinkage is known to entail the formation of macrocracks, which are detrimental to mechanical integrity and performance.[20]

Here, we explore a two-step dealloying strategy similar to ref. [19] but starting from a Ag–Au alloy doped with Pt. The motivation for adding Pt is twofold: First, it is known that

Dr. Z. Qi, Prof. J. Weissmüller
Institute of Materials Physics
Hamburg University of Technology
Eißndorfer Straße 42, 21073 Hamburg, Germany
E-mail: weissmueller@tuhh.de
Dr. U. Vainio
Institute of Materials Research
Materials Physics
Helmholtz-Zentrum Geesthacht
Max-Planck-Straße 1, 21502 Geesthacht, Germany
A. Kornowski, Prof. H. Weller
Institute of Physical Chemistry
University of Hamburg
Grindelallee 117, 20146 Hamburg, Germany
Dr. M. Ritter
Electron Microscopy Unit
Hamburg University of Technology
Eißndorfer Straße 42, 21073 Hamburg, Germany
Dr. H. Jin
Shenyang National Laboratory for Materials Science
Institute of Metal Research
Chinese Academy of Sciences
72 Wenhua Road, 110016 Shenyang, P.R. China
Prof. J. Weissmüller
Institute of Materials Research
Materials Mechanics
Helmholtz-Zentrum Geesthacht
Max-Planck-Straße 1, 21502 Geesthacht, Germany
The copyright line of this paper was amended 20 May 2015 after initial publication.

DOI: 10.1002/adfm.201404544

Pt-doping enables dealloying protocols that create ligament sizes as small as 4 nm,[21,22] considerably less than the ≈15 nm that emerge as (kinetically) stable structures from Ag–Au dealloying. The Pt-containing nanoporous structures are also more resilient to thermal coarsening. Second, recall that high Ag retention, a prerequisite of our two-step dealloying strategy, requires binary Ag–Au master alloys to be dilute in Au and that this entails shrinkage and cracking. It is therefore significant that recent reports point at an unusually high residual Ag fraction when dealloying Pt-doped Ag–Au alloys with higher Au fractions, up to 25 at%.[23–25] Doping with Pt might thus provide a pathway towards mitigating the formation of macro-defects during the synthesis of nested-network nanoporous gold. As the master alloy for this study we therefore chose $Ag_{80}Au_{19}Pt_1$.

2. Results

The preparation strategy for our N^{3}PG samples was closely similar to that of our previous work.[19] The first dealloying step creates nanoporous alloy (designated here as a stage I sample) with a Ag content sufficient for a later, second dealloying step. The microstructure of the nanoporous alloy is then coarsened by thermal annealing, and the resulting material is designated as stage II. The final preparation step is the second dealloying, and samples thus treated are designated as stage III.

The value of the first dealloying potential was selected as follows. By means of chronoamperometry studies at different potentials we identified the lowest potential that gives a steady corrosion current over extended periods of time, that is, the lowest potential that provides a nanoporous structure over the entire sample. This potential, 650 mV, was used in the first step. In order to remove the remaining Ag in the second dealloying step, we referred to ref. [23] and used the potential 1200 mV.

Figure 1 shows scanning electron micrographs of fracture surfaces of samples in each of the three stages, illustrating the interconnected network structure that is characteristic of nanoporous metal. Remarkably, the samples in the stages II and III retain the regular network structure, even though they exhibit a much larger characteristic ligament size. In stage I, the ligament size is ≈22 nm and the composition, as determined by EDS, is characterized by roughly equal atoms fraction of Ag and Au. The high Ag retention is notable, as it provides the basis for the second dealloying step. Annealing establishes the upper hierarchy level ligament size, which Figure 1b shows ≈110 nm.

After the second corrosion, in stage III (Figure 1c), the lower hierarchy level ligaments are expressed. The corresponding ligament size is smaller than what can be observed at this magnification. EDS here suggests a residual Ag fraction of 11 at%.

The insets in Figure 1a–c show macroscopic views of the sample in each stage. Shrinkage was estimated by measuring the projected sample outline in optical micrographs, such as the insets in Figure 1a–c. The volume reduction during the first step was thus determined as 20%; no shrinkage could be detected in the second step. The net shrinkage is here much less than the overall 60% reported in our previous work using dilute Ag–Au master alloys.[19]

A higher magnification SEM image is shown in **Figure 2**. Two well-distinguished structural length scales can here be identified. The characteristic structure size connected with the contrast representing the internal structure of the upper hierarchy level ligaments is ≈6 nm. In view of the dealloying behavior of massive alloys[22] with the same composition as the ligaments of our samples in stages I and II, it is natural to identify the small-scale structure in the interior of the ligaments of Figure 2 with nanoscale porosity. Such an exceptionally small lower hierarchy level ligament size would be in good agreement with the previous studies on conventional NPG doped by Pt[21,22] and it would be considerably smaller than the ≈15 nm of our previous N^{3}PG.[19] Yet, the resolution of the SEM images of Figure 2 is not sufficient for an independent confirmation that the contrast is due to porosity.

In order to scrutinize the nature of the nm-scale structure we performed small-angle X-ray scattering (SAXS) studies. Scattering intensity in SAXS arises from the spatial variation of the electron density which, in the present case, is due to porosity. **Figure 3** shows SAXS results for samples prepared under identical conditions as above. We adopt a representation in a log–log plot of $I \times q^2$ versus q, which emphasizes both interference phenomena and the high-q power-law behavior. For stage I, the SAXS graphs exhibit a clear maximum around $q = 0.29$ nm^{-1}. Equation (1) links this to an average inter-ligament spacing $d = 27$ nm. This is slightly larger than the ligament diameter, $L = 22$ nm, inferred for stage I from the SEM images. The finding $d \gtrsim L$ is not unexpected, since the mean distance between the centers of neighboring ligaments includes also the dimension of the interspersed pore segment.

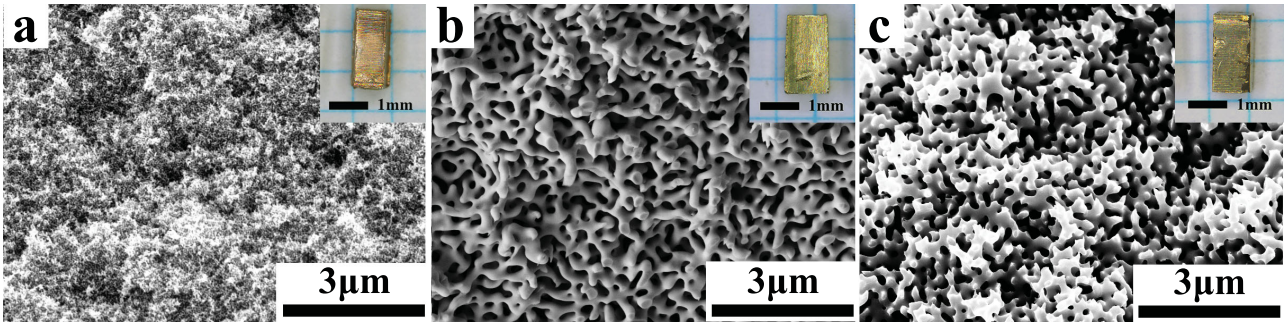

Figure 1. Scanning electron micrographs showing the microstructure on fracture surfaces in each of the three preparation stages. a) Stage I, nanoporous Ag–Au–Pt alloy after dealloying at 650 mV. b) Stage II, after annealing at 400 °C for 0.5 h, illustrating the coarsening. c) Stage III, nested-network structure after the second dealloying step at 1200 mV. Insets in each Figure show the corresponding macroscopic views of the samples.

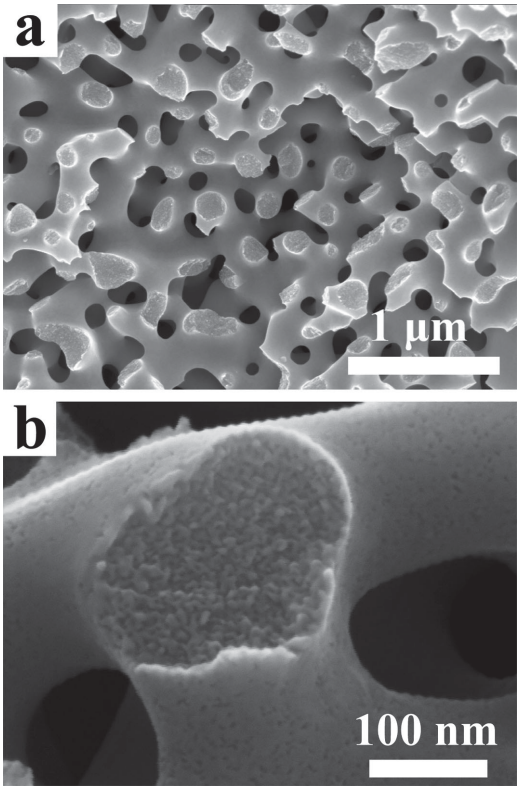

Figure 2. Scanning electron micrographs showing the microstructure of stage III nested-network nanoporous gold. This sample was coarsened at 400 °C for 0.5 h. The overview in a) and the enlarged view in b) show structure on two well-defined length scales. The smaller structure size is ≈6 nm. The serrated edges in b) are due to image drift.

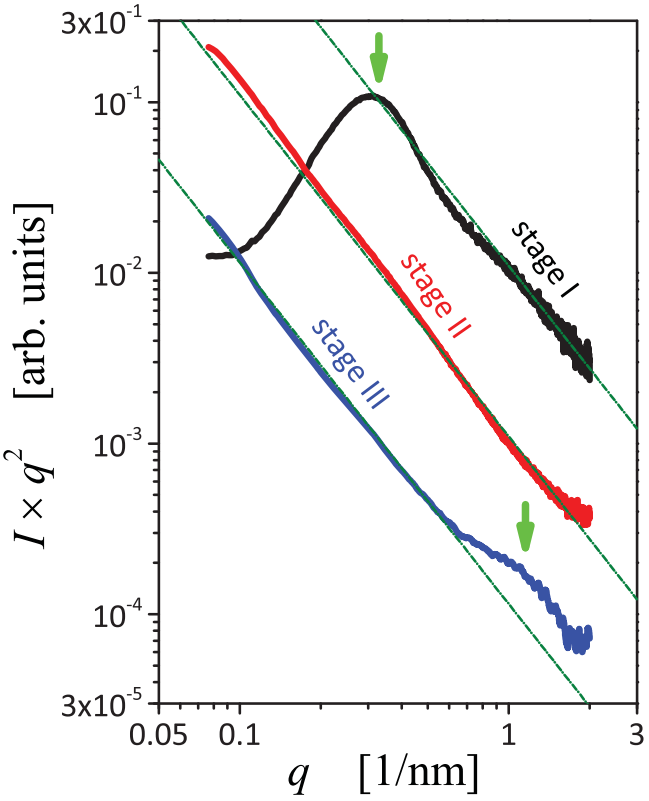

Figure 3. Small-angle X-ray scattering data, showing intensity I multiplied by square of scattering vector magnitude q versus q on log–log scale. Graphs refer to successive stages of synthesis, after initial dealloying (stage I), after subsequent coarsening (stage II), and after conclusive second dealloying step (stage III). Dashed-dotted lines have slope -2 on scale of the graph, illustrating Porod-behavior. Arrows denote interference maxima from initial ligament structure (stage I) and from lower hierarchy level of final nested-network structure (stage III). Coarser structures in stages II and III, forming the upper hierarchy level, are not resolved. Parameters: master alloy $Ag_{80}Au_{19}Pt_1$, first dealloying step at 650 mV, annealing at 400 °C for 0.5 h, second dealloying step at 1200 mV.

The SAXS data are thus in good agreement with the ligament size determined via SEM. Beyond the interference peak, the intensity decays as $I \propto q^{-4}$; this agreement with the Porod law is consistent with the notion of a uniform electron density in the ligaments and with discontinuous surfaces.

The SAXS graph labeled "stage II" refers to the structure after annealing, where the SEM analysis indicates $L = 110$ nm. This ligaments size is outside the resolution of our SAXS experiments, and indeed the scattering data show Porod behavior throughout the entire q-range of Figure 3. However, the signature does again change after the second dealloying process ("stage III"). Figure 3 shows the emergence of an interference maximum in the form of a hump well above the extrapolated Porod part, near the upper q-limit of the experiment. The position of the hump, near $q = 1.2$ nm^{-1}, suggests $d \approx 6.5$ nm. This is again compatible with the SEM structure size of ≈6 nm. The good agreement with Porod's law at the lower q indicates that the structure of the nanoporous network within each upper-hierarchy-level ligament is uniform. The significant insight from the stage III SAXS data is that the second dealloying step indeed creates porosity at the nm scale, so that the contrast in the SEM images of Figure 2 can confidently be attributed to a lower hierarchy level porosity.

One of the attributes of our preparation strategy is that the upper hierarchy level ligament size can be tuned through the annealing treatment in step II. This is exemplified in **Figure 4** for a sample which experienced coarsening at 500 °C for 0.5 h, compared to the 400 °C for the sample presented in Figure 2. The upper hierarchy level ligament size of the 500 °C sample has increased to ≈180 nm. By contrast, at ≈6 nm the lower hierarchy level ligament size remains similar to that of the sample coarsened at 400 °C. Upon close inspection, Figure 4 is seen to confirm a feature that is also discernible in Figure 2, namely, a thin (thickness similar to the lower hierarchy level ligament size) skin at the surface of the upper-level ligaments that is denser than the underlying porous material.

We now turn to an inspection of the crystal structure by means of electron backscatter diffraction (EBSD). **Figure 5**a shows an overview SEM image of a stage III sample with upper hierarchy level ligament size of ≈110 nm. An obvious feature is the homogeneity and integrity of the sample and specifically the absence of cracks. Figure 5b displays an EBSD image, color-coded according to the local orientation in the inverse pole figure, see Figure 5g. In Figure 5b several grains are distinguished by their different orientations. In view of the complex porous microstructure and the extremely small lower hierarchy scale, it is remarkable that the grain size is in the order of tens

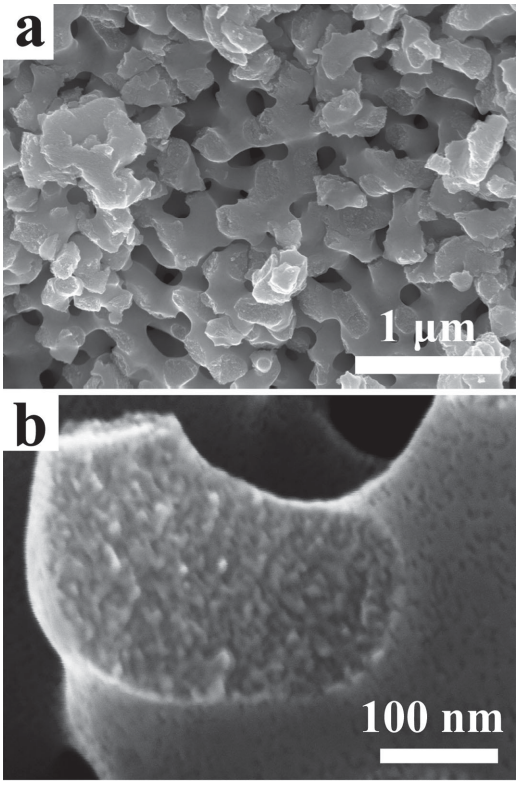

Figure 4. Scanning electron micrographs showing the microstructure of stage III nested-network nanoporous gold. In contrast to Figure 2, this sample was coarsened at the higher temperature of 500 °C for 0.5 h. The overview in a) and the enlarged view in b) show structure on two well-defined length scales.

of micrometers, three to four orders of magnitude larger than the ligaments. The finding of large grain size in our N^3PG samples is in good agreement with previous studies on NPG.[20,26]

Figure 5c,d shows EBSD data of higher magnification for a scanned area of 5×4 µm^2, located entirely within one single grain. Note that the pixel size, 50×50 nm^2, is smaller than the size of upper hierarchy level ligaments, so that their structure is resolved in the EBSD map. Pixels corresponding to pores cannot be indexed, since electrons scattered from the pore bottoms interact with the higher-up ligaments and so do not provide a clear Kikuchi pattern for orientation analysis. The result confirms that the scanned area is from one single grain. The local misorientation map, as shown in Figure 5e, testifies to a very small misorientation within individual grains. The misorientation histogram, Figure 5f, indicates a root-mean-square misorientation of 1.0°.

As a verification of the ordered crystal structure that is suggested by EBSD, we performed wide angle X-ray scattering, using the millimeter-sized samples shown in the insets of Figure 1a–c. The scattering data, **Figure 6**, confirm the face-centered cubic (fcc) crystal structure, showing exclusively fcc Bragg reflections compatible with gold. Because of the large crystal size (≈50 µm, see Figure 5), the number of crystals in the irradiated sample volume is insufficient for a representative X-ray powder diffractogram. As a consequence, the area under the individual reflections does not provide meaningful information on crystallographic texture. Yet, the profiles of the Bragg reflections are significant. In any stage the reflections are well separated. It is seen that reflections become more narrow when stage I samples are transferred to stage II by annealing. This is not unexpected in view of the coarsening of the ligaments. Quite surprisingly, however, the Bragg reflections become even narrower when the second corrosion step transfers the sample to stage III, creating the nanoscale pore structure that forms the first hierarchy level. This observation confirms the high degree of crystalline order in N^3PG that is suggested by the EBSD data.

The lattice parameters, as obtained through Nelson–Riley refinement[27] of the data in Figure 6 for stages I, II, and III are 407.48(5), 407.61(2), and 407.31(2) pm, respectively. These values are slightly less than the lattice parameters of pure Au and Ag, consistent with the presence of the smaller Pt atoms.

3. Discussion

The aim of our study was the preparation of samples of nanoporous gold with a nested-network architecture in which interpenetrating networks of pores and solid ligaments coexist on two distinctly different length scales. Such structures had previously been achieved by a two-step dealloying procedure working with dilute alloys of gold and silver.[19] While bulk samples with controllable sizes of each of the two length scales could indeed be prepared, the earlier results remained limited to lower hierarchy level ligaments not smaller than 20 nm in size. It was thus desirable to extend the range of sizes downwards. Equally important was the strive to enhance the quality of the samples at the macroscopic level. While the earlier synthesis did give uniform hierarchical structures throughout cubic millimeters of sample, significant shrinkage – moderate during the first dealloying step and more severe during the coarsening process – gave rise to a large number of macrocracks. This makes the earlier samples extremely brittle, preventing even the simplest mechanical tests.

The key results of the present study are that (1) Pt addition allows to significantly decrease the size of the lower hierarchy level while at the same time (2) shrinkage is suppressed and the formation of macrocracks mitigated. The net volume shrinkage during the present preparation route is only 20%, considerably less than the 60% of the Ag–Au based approach to N^3PG of ref. [19]. The low shrinkage mitigates crack formation, as is evident from the absence of macrocracks in scanning electron micrographs such as Figure 5a. This supports a high quality of our samples.

We now address the densification on the surface of the upper hierarchy level ligaments that is apparent in Figures 2 and 4. The dense skin might indicate a trend for passivation and, hence, pitting during the annealing step. A more obvious reasoning relates the superficial densification to the general trend of alloy corrosion to produce denser structures near the surface. While coarsening in the interior of a porous crystal, carried by the redistribution of atoms by surface diffusion, leaves the density invariant,[20] diffusion near the surface may involve a net flux of atoms into the interior that increases the density near the surface. The densification involves the removal of lattice planes at the surface as a consequence of the climb of the step edges that provide the sources for the adatoms. In support of

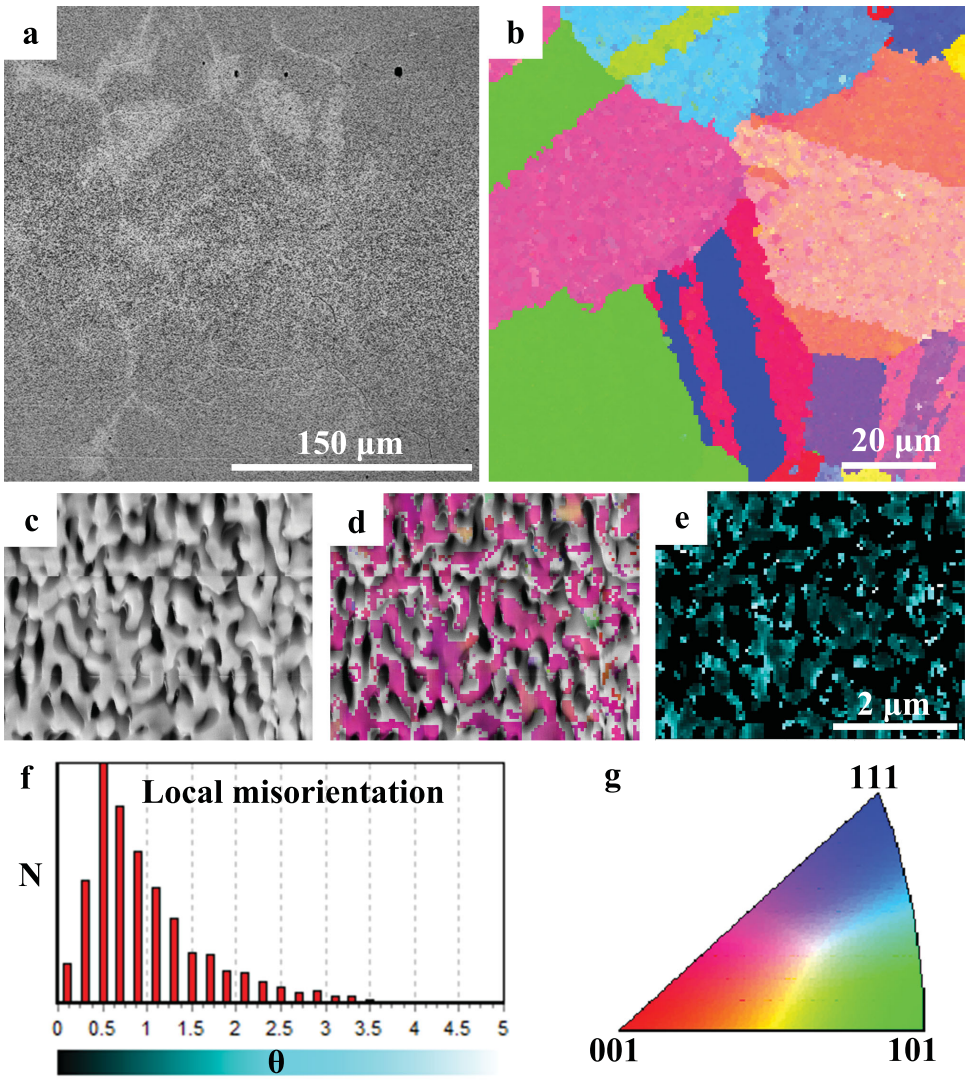

Figure 5. Imaging of nested-network nanoporous gold by scanning electron microscopy (SEM) and electron backscatter diffraction (EBSD). Stage-III sample was dealloyed at 650 mV, annealed at 400 °C for 0.5 h then dealloyed at 1200 mV. a) Overview SEM micrograph. b) EBSD orientation map in inverse pole figure coloring, pixel size 0.5 µm. Note grain size of 20–100 µm. Iterative noise reduction of zero solution was performed. c) SEM micrograph at higher resolution within a single grain. d) EBSD map of area in c), pixel size 0.05 µm. Approximately 45% of the pixels could be indexed. e) Local misorientation map of area in c). f) Local misorientation distribution histogram (misorientation angle, θ, versus fraction, N, of pixels) for data in e). Note that root-mean-square local misorientation is as small as 1.0°, supporting ordered crystal lattice and absence of deformation during preparation by microtome cutting. g) Color code for inverse pole figures.

this reasoning, a densification is found on the surface of nanoporous thin films[28] or single crystals[29] after dealloying. Observations on nanoporous Au nanoparticles[30] are also consistent with this notion.

Our two-step corrosion procedure with an interspersed annealing requires that the first corrosion penetrates the entire master alloy sample while leaving a high residual content of Ag that is required for the later second dealloying step. In the previous work on Ag–Au alloys, we found that this could only be achieved when the original master alloy was dilute (≲10 at%) in Au.[19] It is therefore remarkable that the present alloy achieves the required less noble element retention during the first dealloying step while being much richer in its initial content in more noble element. Similar findings were recently reported,[23–25] along with the following explanation: Much of the Ag dissolution occurs when the ligaments coarsen behind the dissolution front, exposing Ag that was buried in the interior of ligaments during the initial corrosion events. The low mobility of Pt slows down the surface diffusion, thus preventing the coarsening and suppressing the above mechanism of dissolution. The pronounced Pt reduction and hydrogen underpotential deposition peaks which are observed in cyclic voltammetry on nanoporous Au–Pt even for low net Pt content[22,24] as well as spectroscopic data[24] confirm the superficial enrichment in Pt and, thereby, the passivation against further dealloying. The reduced ligament size is well consistent with the reduced surface diffusivity which results from the superficial Pt and with the ensuing suppression of coarsening.[21]

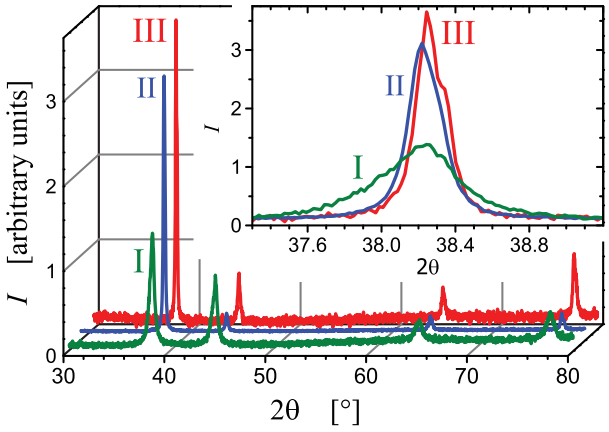

Figure 6. X-ray powder diffraction patterns of scattering intensity *I* versus scattering angle 2*θ*, recorded on millimeters size nanoporous samples such as those in the insets of Figure 1a–c. Preparation stages I, II, and III are indicated by labels. Inset shows the 111-reflections enlarged; note the emerging signature of the $K_{\alpha_{1/2}}$ splitting in stage III, testifying to a narrowing of the peaks during the second dealloying. Intensities have been normalized to unit area under the strongest (namely, the 111-) reflection.

The observation of reduced shrinkage is equally important, and two explanations might be considered. First, at 20 at% the initial gold content in the Pt-doped alloys of the present work is much higher than the 5 at% of the binary Ag–Au of ref. [19]. The present composition is close to what is usually preferred when preparing NPG with good mechanical performance and low volume shrinkage.[4,6,20] Second, in view of the reported correlation of less shrinkage at slower dealloying it is significant that the dealloying of the present ternary alloys is indeed extremely slow. Again, this favors integrity and low crack density.

Our characterization by EBSD and by wide angle X-ray scattering reveals an amazingly high degree of crystalline order in all states of the preparation and specifically in the final N^3PG samples. Coherent crystal lattices are found to extend through tens of µm, so that the ligaments of each of the two structural hierarchy levels, including specifically the extremely small ligaments of the lower level, are part of the same highly ordered face-centered cubic crystal lattice. The misorientation distribution width of a mere 1° as indicated by EBSD is well compatible with the small width of the Bragg reflections in X-ray scattering. While the narrow Bragg reflections may seem unexpected in view of the nanoscale porosity, we emphasize that the long-range (≈50 µm) crystalline coherency is perfectly compatible with narrow interference peaks. The width of the Bragg reflections in stage I may then partly be attributable to microstrain, for instance from defects such as lattice dislocations. Williamson–Hall analysis,[31,32] which might afford quantifying the amount of microstrain, is inapplicable in view of the paucity of irradiated crystallites. We speculate that annealing reduces the dislocation density and that the subsequent second dealloying step allows remaining dislocations to move into the pore space. These pore channel dislocations, which have already been reported in refs. [20,26], keep the regions of largest microstrain – namely, the dislocation cores – in the pore space. Thus, moving dislocations into the pore channels reduces the net amount of microstrain in the solid phase and, thereby, narrows the Bragg reflections.

4. Summary and Conclusion

In summary, we demonstrate that two-step corrosion of Pt-doped Ag–Au is a pathway towards high-quality, macroscopic samples of hierarchical nested-network nanoporous gold. As compared to structures made by dealloying binary Ag–Au,[19] the lower ligament size is decreased and the formation of macrodefects is suppressed. The Pt doped Ag–Au alloy leads to a high Ag retention after the first dealloying step, which is the prerequisite for performing a second dealloying process. As an intermediate step we have shown that the upper hierarchy level ligament size can be modulated by selecting the annealing conditions. The subsequent second dealloying step yields a lower hierarchy level ligament size as small as 6 nm.

The high degree of crystallinity and the long-range order of the crystal lattice of our samples is remarkable. The X-ray as well as electron backscatter diffraction data show that the porous crystallites inherit the highly ordered, crystal lattice structure of the parent alloy, with coherent lattice structures extending tens of micrometers in size. Thus, the corrosion effectively carves out the nanoscale hierarchical ligament structure from macroscopic parent crystals.

Our strategy produces bulk samples free of cracks. This predestines the material as a potential candidate for studies of mechanical properties of hierarchical nanoscale metal structures. The large specific surface area of our samples promotes function, while the large pore cross-section promotes fast transport. The material is thus also a good candidate for applications requiring simultaneously small pores for function and large pores for fast transport, for instance in catalysis and sensing.

5. Experimental Section

Master alloys of $Ag_{80}Au_{19}Pt_1$ were arc melted from pure Ag (99.995%, Chempur), Au (99.995%, Chempur), and Pt (99.95%, Chempur) in a Ti-gettered Ar (99.9995%) atmosphere. For homogeneity, we first prepared an intermediate Au–Pt alloy and only added Ag in a later, separate melting process comprising several melting/solidification cycles. The ingots were homogenized for more than 100 h at 950 °C in evacuated and sealed quartz tubes, followed by quenching in water to prevent phase separation. Cuboid samples, 1 × 1 × 2 mm^3 in size, were cut from the quenched ingots using a diamond wire saw.

The cuboids were dealloyed at room temperature (≈20 °C) under potential control in 1 M $HClO_4$ (Superpur, Merck). Electrochemical dealloying used a three-electrode setup controlled by a potentiostat (Autolab, PGSTAT100N). The Pt wire counter electrode shared the cell (volume 300 mL) with the working electrode. Potentials were measured and are here specified relative to Ag/AgCl pseudo-reference electrodes in the same solution (530 mV positive versus the standard hydrogen electrode).

The dealloying potential was 650 mV in the first step and was maintained until the current decayed to 10 µA. The samples were then rinsed repeatedly in ultrapure water (18 MΩ cm, Arium 611, Sartorius) and finally in alcohol (ACS grade, Merck), followed by drying in a glove box under Ar atmosphere. The second dealloying step used the same setup and the potential was 1200 mV. The intermediate coarsening treatments were done in a vacuum furnace (10^{-6} mbar) at 400 or 500 °C for 0.5 h.

For structural characterization, scanning electron microscopes (SEMs) Zeiss Supra VP55 and Leo 1550 at accelerating voltages of 10–20 kV, partly combined with energy dispersive (EDS) and wavelength-dispersive (WDS) X-ray spectroscopy were used. Note that EDS is poorly suited for quantifying the Pt fraction due to overlap of the Au and Pt

fluorescence lines. More quantitative information could be obtained by WDS. For the master alloy samples, WDS typically indicated uniform composition with values around $Ag_{79.3}Au_{19.9}Pt_{0.8}$. This is consistent with the nominal alloy composition and suggests a uniform alloy microstructure and composition before corrosion.

Samples for electron backscatter diffraction (EBSD) measurements in the SEM were prepared using ultramicrotomy (Leica UC7) as follows. The mm-sized porous metal samples were infiltrated with low viscosity epoxy (EpoThin, Buehler). After hardening overnight, a trimming knife was used to form a pyramidal shape terminating in a block face of approximately 300 × 300 μm^2. Several thin sections of about 20–50 nm thickness were cut away with a diamond knife (Diatome Ultra 45°, 1.5 mm) at a cutting speed of 1 mm s^{-1}, before the block face was used for EBSD. EBSD measurements were carried out at a block face inclination angle of 70° using 80 ms dwell time and a 1.4 nA beam at 20 kV in a Zeiss Supra VP55 with an Oxford HKL Nordlys EBSD system.

We also characterized the samples by wide-angle X-ray scattering, using a powder diffractometer (Bruker D8) in focusing Bragg–Brentano, θ–θ geometry with a sealed Cu anode, a Ni filter in the diffracted beam, and a linear position-sensitive detector. The cuboid samples were measured in as-prepared size and shape, with diffraction from the top side.

Small-angle X-ray scattering (SAXS) was measured using a Bruker NanoStar setup with a IμS microfocus X-ray source (Cu anode) and a VÅNTEC area detector. Scattering angles were calibrated by means of a silver behenate standard and converted to scattering vector magnitude, q, using $q = 4\pi\sin\theta/\lambda$, where θ denotes half of the scattering angle and λ represents the wavelength. The resolved q-range was 0.08 nm^{-1} ≤ q ≤ 2 nm^{-1}. The well-defined structural length scale of nanoscale network structures made by dealloying is known to give rise to an interference peak in small angle scattering[33,34] that is reminiscent of interference in spinodally decomposed fluids.[35] A simple estimate for the characteristic spacing between ligaments in the network may be obtained from the Debye formula for the interference in a set of randomly oriented pairs of scatterers with a characteristic distance d. The formula links d to the value, q_{max}, of q at the maximum of the interference peak via[36]

$$q_{max} \approx 1.23\frac{2\pi}{d} \quad (1)$$

The q-range of our study thus translates into a resolution of structure sizes in the order of 4–100 nm. X-ray transparent samples were obtained by crushing the nanoporous bodies through gentle grinding in a mortar, followed by spreading of the powder on adhesive tape. The nonuniform thickness of the samples prevented a meaningful reduction of the scattering intensities to absolute units.

Acknowledgements

Support by Chinese Scholarship Council (Z. Qi) and by Deutsche Forschungsgemeinschaft (SFB 986 'M^3' projects B2, C6, Z2, and Z3) is gratefully acknowledged. We thank Mr. Jens Timmermann and Mrs. Lida Wang at the Electron Microscopy Unit, Hamburg University of Technology for assistance with SEM imaging and sample preparation.

Received: December 22, 2014
Revised: February 1, 2015
Published online: March 16, 2015

[1] R. Li, K. Sieradzki, *Phys. Rev. Lett.* **1992**, *68*, 1168.
[2] J. Erlebacher, M. J. Aziz, A. Karma, N. Dimitrov, K. Sieradzki, *Nature* **2001**, *410*, 450.
[3] N. A. Senior, R. C. Newman, *Nanotechnology* **2006**, *17*, 2311.
[4] J. Weissmüller, R. C. Newman, H. J. Jin, A. M. Hodge, J. W. Kysar, *MRS Bull.* **2009**, *34*, 577.
[5] Z. H. Zhang, Y. Wang, Z. Qi, W. Zhang, J. Qin, J. Frenzel, *J. Phys. Chem. C* **2009**, *113*, 12629.
[6] F. Kertis, J. Snyder, L. Govada, S. Khurshid, N. Chayen, J. Erlebacher, *JOM* **2010**, *62*, 50.
[7] D. Kramer, R. N. Viswanath, J. Weissmüller, *Nano Lett.* **2004**, *4*, 793.
[8] C. X. Xu, J. X. Su, X. H. Xu, P. P. Liu, H. J. Zhao, F. Tian, Y. Ding, *J. Am. Chem. Soc.* **2007**, *129*, 42.
[9] J. Biener, A. Wittstock, L. A. Zepeda-Ruiz, M. M. Biener, V. Zielasek, D. N. Kramer, R. Viswanath, J. Weissmüller, M. Bäumer, A. V. Hamza, *Nat. Mater.* **2009**, *8*, 47.
[10] Y. Ding, M. W. Chen, *MRS Bull.* **2009**, *34*, 569.
[11] X. Lang, A. Hirata, T. Fujita, M. Chen, *Nat. Nanotechnol.* **2011**, *6*, 232.
[12] T. Fujita, P. F. Guan, K. McKenna, X. Y. Lang, A. Hirata, L. Zhang, T. Tokunaga, S. Arai, Y. Yamamoto, N. Tanaka, M. W. Chen, *Nat. Mater.* **2012**, *11*, 775.
[13] Y. Ding, J. Erlebacher, *J. Am. Chem. Soc.* **2003**, *125*, 7772.
[14] J. Biener, G. W. Nyce, A. M. Hodge, M. M. Biener, A. V. Hamza, S. A. Maier, *Adv. Mater.* **2008**, *20*, 1211.
[15] Z. H. Zhang, Y. Wang, Z. Qi, J. K. Lin, X. F. Bian, *J. Phys. Chem. C* **2009**, *113*, 1308.
[16] Z. H. Zhang, Y. Wang, X. G. Wang, *Nanoscale* **2011**, *3*, 1663.
[17] S. Sattayasamitsathit, A. M. O'ahony, X. Y. Xiao, S. Brozik, C. M. Washburn, D. R. Wheeler, W. Gao, S. Minteer, J. Cha, D. B. Burckel, R. Polsky, J. Wang, *J. Mater. Chem.* **2012**, *22*, 11950.
[18] M. N. Lee, M. A. Santiago-Cordoba, C. E. Hamilton, N. K. Subbaiyan, J. G. Duque, K. A. D. Obrey, *J. Phys. Chem. Lett.* **2014**, *5*, 809.
[19] Z. Qi, J. Weissmüller, *ACS Nano* **2013**, *7*, 5948.
[20] S. Parida, D. Kramer, C. A. Volkert, H. Rösner, J. Erlebacher, J. Weissmüller, *Phys. Rev. Lett.* **2006**, *97*, 035504.
[21] J. Snyder, P. Asanithi, A. B. Dalton, J. Erlebacher, *Adv. Mater.* **2008**, *20*, 4883.
[22] H. J. Jin, X. L. Wang, S. Parida, K. Wang, M. Seo, J. Weissmüller, *Nano Lett.* **2010**, *10*, 187.
[23] X. L. Ye, N. Lu, X. J. Li, K. Du, J. Tan, H. J. Jin, *J. Electrochem. Soc.* **2014**, *161*, C517.
[24] A. A. Vega, R. C. Newman, *J. Electrochem. Soc.* **2014**, *161*, C1.
[25] A. A. Vega, R. C. Newman, *J. Electrochem. Soc.* **2014**, *161*, C11.
[26] H. J. Jin, L. Kurmanaeva, J. Schmauch, H. Rösner, Y. Ivanisenko, J. Weissmüller, *Acta Mater.* **2009**, *57*, 2665.
[27] L. Schwartz, J. Cohen, *Diffraction from Materials*, Academic Press, New York NY **1977**.
[28] Y. Sun, K. P. Kucera, S. A. Burger, T. J. Balk, *Scr. Mater.* **2008**, *58*, 1018.
[29] A. Pareek, S. Borodin, A. Bashir, G. N. Ankah, P. Keil, G. A. Eckstein, M. Rohwerder, M. Stratmann, Y. Gründer, F. U. Renner, *J. Am. Chem. Soc.* **2011**, *133*, 18264.
[30] X. Q. Li, Q. Chen, I. McCue, J. Snyder, P. Crozier, J. Erlebacher, K. Sieradzki, *Nano Lett.* **2014**, *14*, 2569.
[31] H. P. Klug, L. E. Alexander, *X-Ray Diffraction Procedures*, Wiley, New York **1974**.
[32] J. Markmann, V. Yamakov, J. Weissmüller, *Scr. Mater.* **2008**, *59*, 15.
[33] D. V. Pugh, A. Dursun, S. G. Corcoran, *J. Mater. Res.* **2003**, *18*, 216.
[34] C. J. Dotzler, B. Ingham, B. N. Illy, K. Wallwork, M. P. Ryan, M. F. Toney, *Adv. Funct. Mater.* **2011**, *21*, 3938.
[35] N. F. Berk, *Phys. Rev. Lett.* **1987**, *58*, 2718.
[36] A. Michels, J. Weissmüller, *Rep. Prog. Phys.* **2008**, *71*, 066501.